Encyclopedia of Nanotechnology
DOI 10.1007/978-94-007-6178-0_100915-1

Physics in Laser Near-Field Nanomanufacturing: Fundamental Understanding and Novel Probing

Shen Xu[a], Lijun Zhang[b], Yanan Yue[c] and Xinwei Wang[d]*
[a]Department of Mechanical Engineering, Iowa State University, Ames, IA, USA
[b]Department of Mechanical Engineering, Shanghai Ocean University, Shanghai, People's Republic of China
[c]School of Power and Mechanical Engineering, Wuhan University, Wuhan, Hubei, People's Republic of China
[d]Department of Mechanical Engineering, Iowa State University, Ames, IA, USA

Synonyms

Laser-assisted tip-based heating and fabrication; Laser-assisted tip–substrate interaction; Near-field focusing and heating

Definition of the Subject

Laser near-field nanomanufacturing is manufacturing nanoscaled materials and complex structures at the nanoscale by means of phase change/explosion with the near-field focused laser beam, whose spot size is usually smaller than its wavelength.

Introduction

Nanofabrication and nanomanufacturing involve manufacturing of materials, structures, devices, and systems down to the nanoscale. There are two basic categories of fabrication, top-down and bottom-up or self-assembly processes, containing a growing number of chemical and physical techniques, such as chemical methods, chemical vapor deposition, molecular beam epitaxy, atomic layer epitaxy, lithography, self-assembly, and countless newly developed techniques. Among those methods, laser-assisted nanomanufacturing plays an important role due to its highly coherent feature. To achieve a resolution below the diffraction limit, various near-field mechanisms of laser-assisted technologies have been developed in past decades, such as the laser-assisted nanopatterning and nanoimprinting lithography, near-field scanning optical microscopy (NSOM), superlens, nanoscale aperture, and scanning probe microscopes (SPM).

The laser-assisted tip-based fabrication is a large branch of laser-assisted manufacturing techniques by using SPM tips. The SPM tip is an ideal tool for apertureless NSOM due to its tiny but sharp geometry. When a laser irradiates the SPM tip, it can bend the propagation direction of the laser and focus and enhance the optical field in an extremely small area in proximity to the tip apex. The enhancement factor could be more than 100 by using a scanning tunneling microscope (STM) tip. This strongly enhanced optical field is then utilized to develop a new fabrication method by using laser-irradiated STM tip [1]. The absorption of this enhanced optical field could generate heat in the sample surface and induce phase change at the nanoscale, finally modifying the surface. Similar to STM, atomic force microscopes (AFM) can focus the laser beam to a nanoscale spot as well to achieve surface manufacturing at the nanoscale.

*Email: xwang3@iastate.edu

DOI 10.1007/978-94-007-6178-0_100915-1

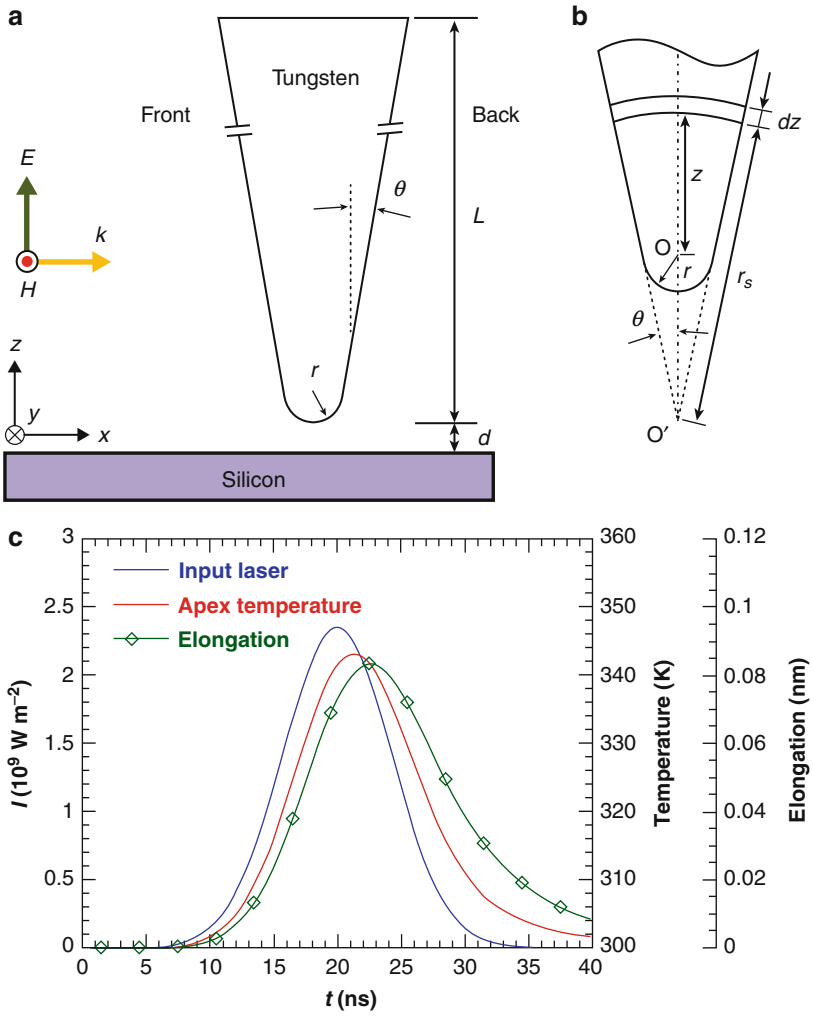

Fig. 1 (**a**) Schematic of the tip–substrate system, (**b**) geometric structure of the tip model, and (**c**) the temperature evolution against the time (Reprinted from ref. [2], © IOP Publishing. Reproduced by permission of IOP Publishing. All rights reserved)

This entry focuses on experimental and computational works about laser-assisted SPM nanostructuring. Section Near-Field Focusing and Heating by the Micro/Nanoscale AFM Tip: Effect on the Tip introduces experiment and simulation of the temperature and optical field distribution in the AFM tip when it is heated by near-field focusing laser. Section Near-Field Focusing and Heating by the Micro/Nanoscale AFM tip: Effect on the Substrate discusses the study about the temperature measurement and optical field distribution simulation in a silicon substrate next to the apex of the AFM tip. Sections Near-Field Focusing by Micron/Submicron Particles: Experimental Study and Near-Field Thermal, Optical, and Mechanical Phenomena: Modeling are for experiments and simulation study, respectively, for the near-field thermal, optical, and mechanical phenomena of a silicon plate under the micro/submicron particles. Section Material Structure Evolution Under Near-Field Laser Heating mainly focuses on the simulation work about material's structure change under near-field laser heating, including structure evolution and the effect of shock waves.

Encyclopedia of Nanotechnology
DOI 10.1007/978-94-007-6178-0_100915-1

Near-Field Focusing and Heating by the Micro-/Nanoscale AFM Tip: Effect on the Tip

The enhanced optical distribution in and around the apex of a tip has been widely studied. The thermal evolution and thermal distribution, however, was studied little. Chen et al. [2] has conducted high fidelity and systematic simulation of near-field thermal transport in an AFM tungsten tip under laser irradiation. The electromagnetic field and temperature distribution is simulated in a domain housing a tungsten SPM tip and silicon substrate system.

FEM Modeling for Both Optical and Thermal Physics in AFM Tip Under Irradiation

The model (Fig. 1a) employs a conical tungsten tip ended with a hemisphere on the silicon substrate. The modeling is performed by using a high-frequency structure simulator (HFSS V12.1 ANSYS, Inc.), a full-wave high-frequency 3-D finite element modeler of Maxwell's equations. Maxwell's equations are solved across the vacuum domain. Tetrahedral elements with a length shorter than one-fourth of the incident wavelength are set in the whole domain. They are further refined in areas where the high field gradient may occur. Absorbing boundaries are applied for the domain. The incident plane wave is along the x direction of the tip.

The geometry of the tip is shown in Fig. 1b. The length L of the tip model is carefully chosen as 600 nm which is a good approximation of 15 μm long commercial tips. The tip apex radius $r = 30$ nm and the half taper angle $\theta = 10°$ are used in the simulation. The distance d between the tip and substrate is set as 5 nm. The Poynting vector simulation illustrates the incident laser is bent around the tip and concentrated under the apex, and the extremely intensive electric field appears there. The largest enhancement factor around 15 under the apex in the model is given by the electric field simulation. In contrast, the electric field is much less enhanced inside the tip, since only a small fraction of laser penetrates into the tip. The electric field is not symmetrical inside the tip. Its gradient decreases along the laser's incident direction.

Three factors significantly affect the electric field enhancement: the laser polarization direction, the geometry of the tip, and the distance between the tip apex and the substrate. The intensity enhancement of the electric field depends on $\cos^2\varphi$, where φ is the polarization angle to the tip axis. Only the component along the tip axis of the incident laser makes a contribution to the electric field enhancement under the tip apex. For the geometry factor, the optimum r for electric field enhancement is about 9 nm when the half taper angle θ is 10°. For a tip with a fixed radius of 30 nm, the field enhancement first increases along with θ increasing when θ is less than 25°, and the field enhancement keeps pretty much constant in the range of 25–30° and then decreases as θ goes beyond 35°. Moreover, the peak field enhancement decreases exponentially as the tip–substrate distance increases, and a shift of field peak position is observed being away from the tip axis. This shift vanishes when the tip touches the substrate.

A single pulse is applied on the tip to study the temperature evolution and distribution in the tip at room temperature (300 K). The simulation of the temperature distribution in the tip is conducted with commercial computational software FLUENT (V12.0.1 ANSYS, Inc.). The intensity of the electric field is calculated according to the Poynting vector. The maximum temperature in the tip apex is delayed (Fig. 1c) due to the thermal conduction in the tip when compared with the maximum energy in the laser pulse. The resulting temperature distribution is affected by two factors: the heat source due to laser absorption and the geometric shape of the tip. As the polarization angle or apex radius increases, the peak apex temperature decreases. The half taper angle strongly affects the thermal transport in the tip. The peak apex temperature declines with an increased taper angle, even though the laser intensity inside the tip is increasing in the meanwhile.

DOI 10.1007/978-94-007-6178-0_100915-1

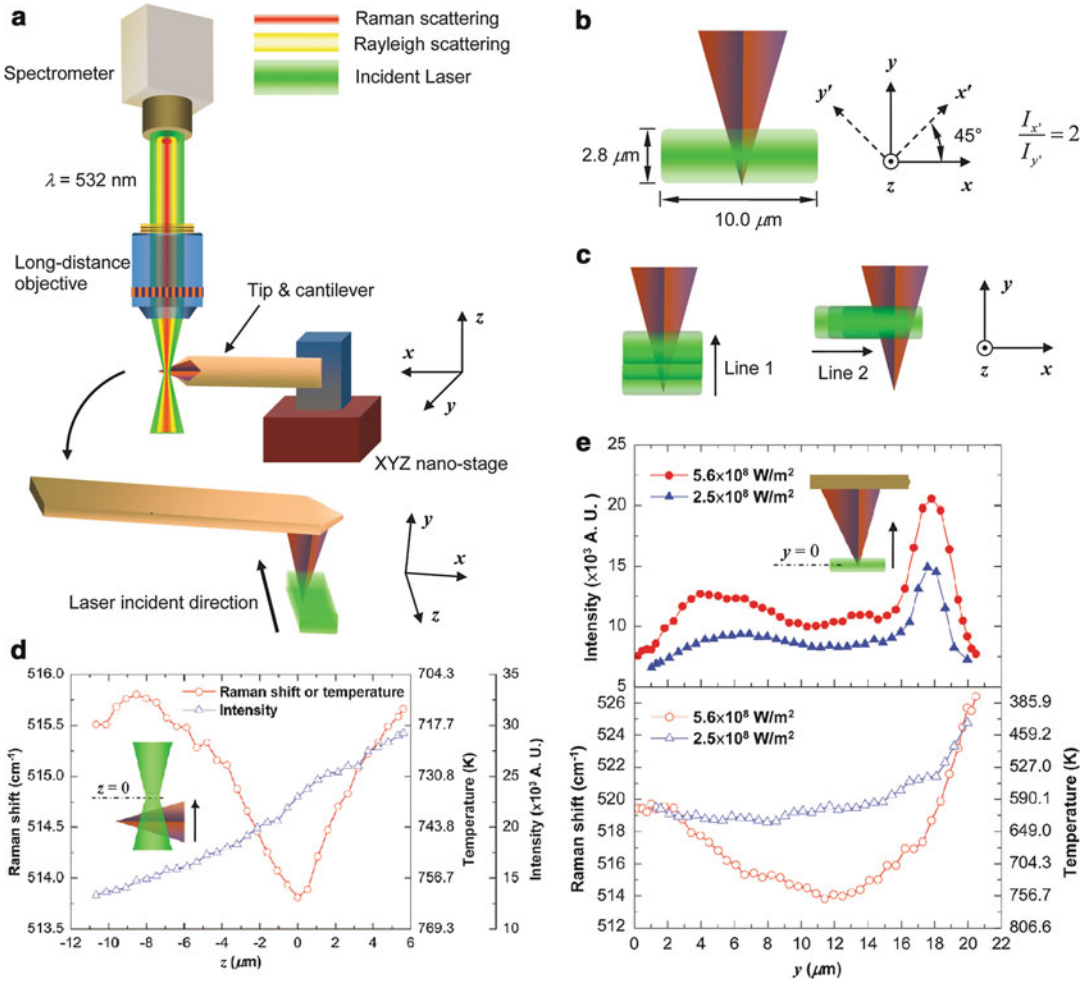

Fig. 2 (**a**) Schematic of experimental setup (no to scale). (**b**) Configuration of the laser beam at the focal spot when the laser illuminates the side surface of tip. (**c**) Laser spot moving directions with respect to the tip during experiment. (**d**) Raman shift, temperature, and Raman intensity when the tip moves upward along the *z* direction in the vicinity of focal spot. (e) Raman intensity and Raman shift along line 1 [as shown in Fig. 2c, in the *y* direction] under energy fluxes of 5.6×10^8 and 2.5×10^8 W/m^2, respectively (Reprinted from ref. [3], © IOP Publishing. Reproduced by permission of IOP Publishing. All rights reserved)

Experimental Details of Temperature Measurement in the AFM Tip

The corresponding experimental work is conducted with a freestanding AFM silicon tip [3] under the laser irradiation with a micrometer spatial resolution. A single crystal silicon (antimony doped) tip (CSG10, K-Tek nanotechnology) is mounted on a three-dimensional piezo-actuated nanostage with a positioning resolution of 20 nm. The stage with the sample is placed under the laser spot at the focal level of a confocal Raman microscope system (Voyage, B&W Tek, Inc.). The tip axis is horizontal and along the *y* direction of the nanostage. The cantilever is along the *x* direction, and the laser is incident vertically along the *z* direction. The whole system is placed in air. The laser beam is focused through a 20× microscope objective (NA = 0.40, WD = 12.0 mm) with a focal spot size of 2.8×10.0 μm^2. The laser beam is partially polarized along the *x*' and *y*' directions as shown in Fig. 2b. The nanostage is aligned to make sure that the laser is coming in along the *z* direction. The tip axis is perpendicular to the longer side of the laser spot. In this case, the tip axis has an angle of 45° with respect to the direction in which the polarized laser has the strongest intensity. The laser with a wavelength of 532 nm is used as both Raman

DOI 10.1007/978-94-007-6178-0_100915-1

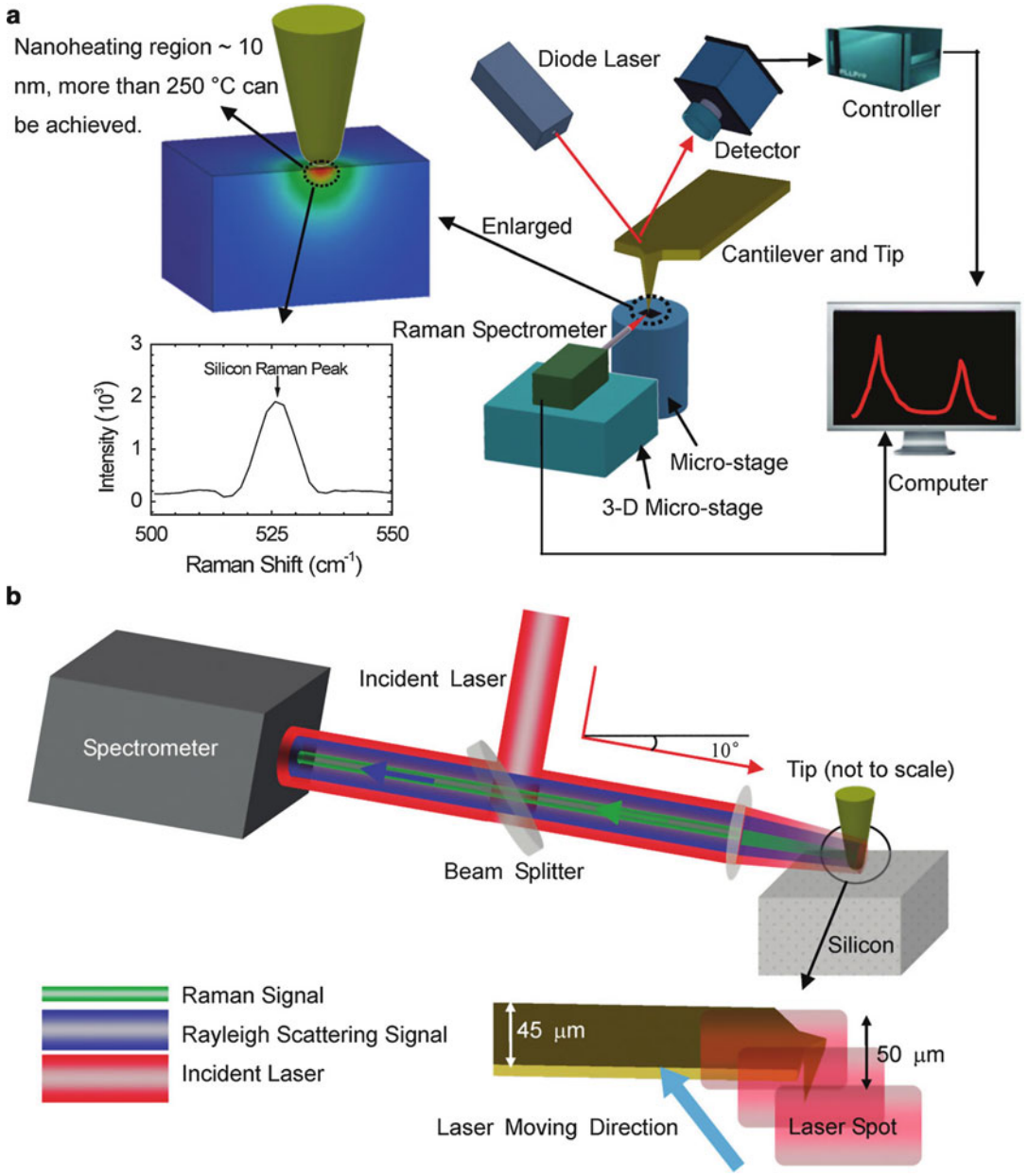

Fig. 3 (**a**) Schematic of experimental setup for the apertureless NSOM (not to scale) for thermal sensing. (**b**) Schematic of the optical system. The incident laser passes through a beam splitter and is focused on the tip by a convex lens. The excited Raman signal and Rayleigh scattering signal go along the same optical trace back to the spectrometer (Reprinted with permission from ref. [5], Copyright (2011) American Chemical Society)

probe and heat source. To investigate the heating effect caused by laser, the tip is illuminated with different laser powers of 4, 7, 12.7, and 15.9 mW.

The Raman shift method of Raman thermometry is used to determine the temperature rise of the Si AFM tip under laser irradiation. Raman shift will become smaller when the temperature of the probing area goes up. The exact temperature rise is then calculated based on the theoretical calculation introduced by McCarthy et al. [4]. To precisely extract the Raman shift, the silicon Raman peak in all measured spectra is fitted with the Gaussian function. In order to exclude the focusing effect on the experimental

DOI 10.1007/978-94-007-6178-0_100915-1

result, the diffraction image of the tip under laser illumination is examined to precisely monitor the focusing level.

The temperature rise in the tip is first studied as the tip moves along the *z* direction, and the whole travel covers the focal spot (Fig. 2d). When the tip moves upward closer to the focal spot, the Raman shift decreases and the temperature increases; analogously, when the tip passes the focal spot and keeps moving upward, the Raman shift increases and the temperature goes down. Nevertheless, the Raman intensity increases during the whole process. When the laser spot is moved along the tip axis at the focal level from tip apex to cantilever, the temperature in the tip increases first and then decreases (Fig. 2e). The corresponding temperature increases from 603 to 754 K and then declines to 728 K. This is a trade-off between the increasing of laser absorbing area and the increasing heat conduction to the base of the tip even the cantilever. The incident laser intensity also strongly affects the heating condition.

To investigate the mechanism of the near-field heating in the experiment, the electric field distribution around the tip and inside the tip is calculated using the similar method as described in section FEM Modeling for Both Optical and Thermal Physics in AFM tip Under Irradiation. The highest field enhancement is 5.19 and 2.86 for under the tip apex and inside the tip, respectively. A one-dimensional heat transfer model is used to calculate the temperature distribution along the tip axis. Details of the calculation can be found in the reference [3]. The highest temperature of 448 K is obtained at the hemisphere apex from the calculation, while the measured temperature is approximately 600 K. The difference between them could be induced by further thermal conductivity reduction of the Si tip by its dopants and the underestimated laser scattering/absorption in the tip.

Near-Field Focusing and Heating by the Micro-/Nanoscale AFM Tip: Effect on the Substrate

According to Chen's study, an AFM tip can induce the near-field enhancement on electromagnetic field next to the tip apex when an external laser irradiates the tip. Besides, the local heating in the substrate beneath the tip can also induce a considerable temperature rise. The first experimental work for the direct temperature measurement was done by Yue et al. [5]. The Raman shift method is applied to measure the temperature variation in a sub-10 nm area of the silicon substrate beneath the apex of the AFM tip.

Experimental Details

Before the temperature measurement, thermal response calibration is conducted between Raman shift of Si peak and temperature from room temperature to 230 °C. A silicon sample is heated using a power-adjustable electrical heater and temperature is sensed by a T-type thermocouple. The Raman signals are excited by using the 785 nm probing laser from the Raman spectrometer (B&W Tek). The Raman spectra are then fitted with the Gaussian function to obtain precise Raman shift of the Si peak. The obtained linear relationship between Raman shift and temperature is used to determine the temperature in the substrate in the experiment.

The experimental setup is shown in Fig. 3. A silicon substrate is mounted on a 3-D nanostage in the AFM system, and the 20 nm gold-coated AFM silicon tip is fixed above the substrate. A Raman spectrometer (B&W Tek) is mounted on another 3-D microstage and placed in front of the fixed AFM tip–substrate system. A beam splitter and a lens are placed on the optical path between Raman probe and the tip. The incident Raman laser is focused on the tip by using the lens, and the reflected incident laser is then used to monitor the irradiating position. The incident angle with respect to the tip axis is kept to be around 80° in order to reduce the Raman signal directly from the unheated silicon. Three cases with three different polarized angles, 15°, 30°, and 75° (with respect to the tip axis), are studied. In 15° and 30° cases,

DOI 10.1007/978-94-007-6178-0_100915-1

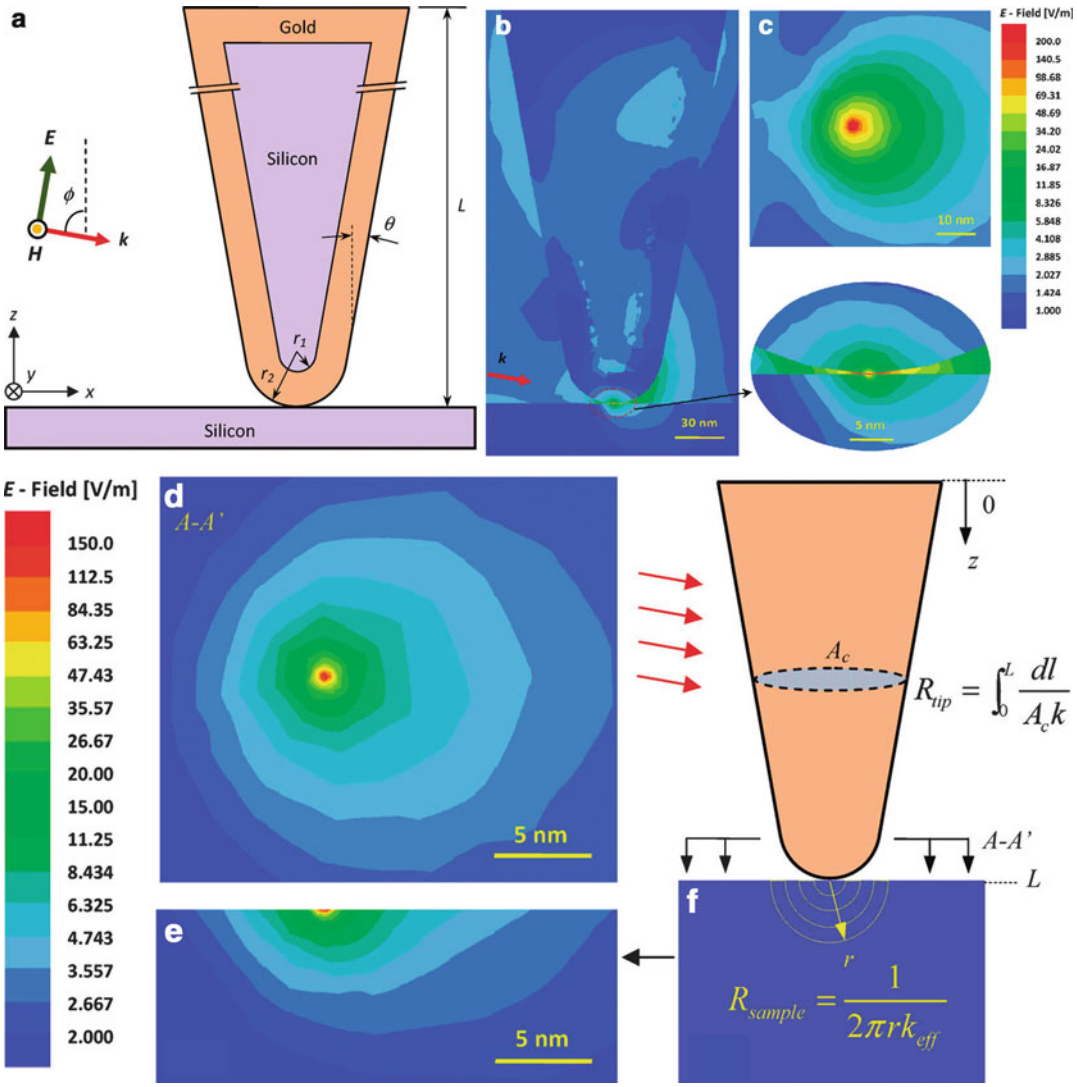

Fig. 4 (**a**) Schematic of tip–substrate model in the simulation. Electric field distribution around the tip for (**b**) front view in the $y = 0$ plane and (**c**) top view of the cross section under the tip apex under vacuum. (**d**) The electric field distribution in the A-A' plane, (**e**) cross-sectional view of the distribution, and (**f**) schematic of the thermal resistance calculation of the tip and Si substrate (Reprinted with permission from reference [5], Copyright (2011) American Chemical Society)

the temperature rise is more than 200 °C in the sub-10 nm area in the silicon substrate due to the near-field focus effect next to the AFM tip apex.

Simulation Study of the Near-Field Optical Effect and Thermal Effect

The simulation of corresponding electric field enhancement is also conducted to well explain the mechanism behind the above experiment. The HFSS (V13 ANSYS, Inc.) is used for calculating the electric field distribution in a tip–substrate system. The simulated model is shown in Fig. 4a: a well-defined rectangular domain contains a 20 nm gold-coated silicon tip and a 200 nm thick silicon substrate. The length L of the tip in the model is 600 nm, the half taper angle θ is 10°, and the apex radius r_1 is 10 nm. The polarized laser illuminates the tip along the x direction with an incident angle ϕ of 80° to the z direction. The simulation result (Fig. 4b–f) shows a large enhancement of the electric field only in the vicinity of the contact point between the tip and substrate. This extremely strong electric field focuses into a hemisphere with a diameter of sub-10 nm in the silicon substrate.

DOI 10.1007/978-94-007-6178-0_100915-1

Nonlinear Optical Absorption and Ballistic Heat Conduction in the Near-Field Focused Region in the Substrate

To calculate the temperature rise in the near-field heating region, a thermal model is established as $\int_{\Delta V} I\beta\, dv = (T - T_\infty)/R_{\text{th}}$ which means an equilibrium between heat generation from the enhanced electric field and heat transfer from the heating region to the outside. ΔV is the near-field heating domain ($\Delta V \approx 2\pi r_e^3/3$). r_e is the effective radius of this heating region. It can be derived from nonlinear photon absorption induced by the high intensity of the optical field in the silicon. The electric field under the tip is first enhanced due to the near-field effect on the incident laser. This enhanced electric field then excites the tip again which contributes to an additional radiated electric field enhancement. Both enhancements of the electric field by the incident laser and the excited tip are second order; meanwhile, they are symmetrical in the same wavelength. Therefore, the overall magnitude of the intensity would be $\sim M^4$ [6]. M is the magnitude of enhanced electric field. The optical field intensity under low polarization angles (15° and 30°) is as high as 10^{14} W/m^2 within a 1 nm radius hemispherical region in silicon. The avalanche ionization process then occurs due to the short absorption depth (75 nm) in this region [6], where the electrical field intensity exceeds the threshold. Thus, the effective radius r_e of the hemisphere region is calculated as 0.8 nm in the case of 15° polarization angle.

To calculate the theoretical temperature rise, the thermal resistance from the heating region to the outside is also needed. R_{th} is expressed as $1/(2\pi r_e k_{\text{eff}})$, where k_{eff} is the local effective thermal conductivity. k_{eff} is determined by considering the strong ballistic heat transfer effect due to the extremely small heating region. This heating domain (within 10 nm scale) is even smaller than the mean free path of silicon as 43 nm at room temperature. Thermal equilibrium cannot be achieved because of not enough scattering and collisions of phonons [7]. The thermal conductivity (k_{eff}) is then used for the heating region in silicon, which can be expressed as $3k/(3 + 4\tau)$, where k is the thermal conductivity of bulk silicon, and $\tau = r/\Lambda$, where Λ is the mean free path of the phonon in bulk silicon. The effective thermal conductivity is evaluated as 2.5 W/(m·K) in the calculation region. Thus, the temperature rise in this sub-10 nm domain is calculated as 235 °C and 105 °C for the 15° and 30° cases, respectively, which agree well with the experimental result. For the 75° case, a very weak optical field intensity enhancement occurs, and the temperature rise is negligible.

Near-Field Focusing by Micron/Submicron Particles: Experimental Study

Micro-/nanoparticle is another kind of useful geometry for inducing ultra-focusing and heating into sub-wavelength. This technique has been widely used in laser-assisted nanopatterning and nanolithography on a large-area substrate. Knowledge of the temperature and stress in the nanoscale beneath the particles is critical for process control and optimization. At present, the extremely small size of this heating area (~100 nm or less) remains a big challenge for nanoscale temperature, stress, and optical field probing because the heating area is very small and not immediately accessible for sensing. Tang et al. [8–10] did the pioneering and systematic experimental study of the effects of temperature, stress, and near-field focusing in the silicon plate under a single silica particle, a glass fiber, and a layer of particles, with Raman spectroscopy.

Experimental Details

The sample is prepared by spreading a single layer of glass nanoparticle mixture on a clean silicon wafer using a tilting technique. Different sizes of particles, 200, 400, 800, and 1,210 nm (diameters), are used.

Encyclopedia of Nanotechnology
DOI 10.1007/978-94-007-6178-0_100915-1

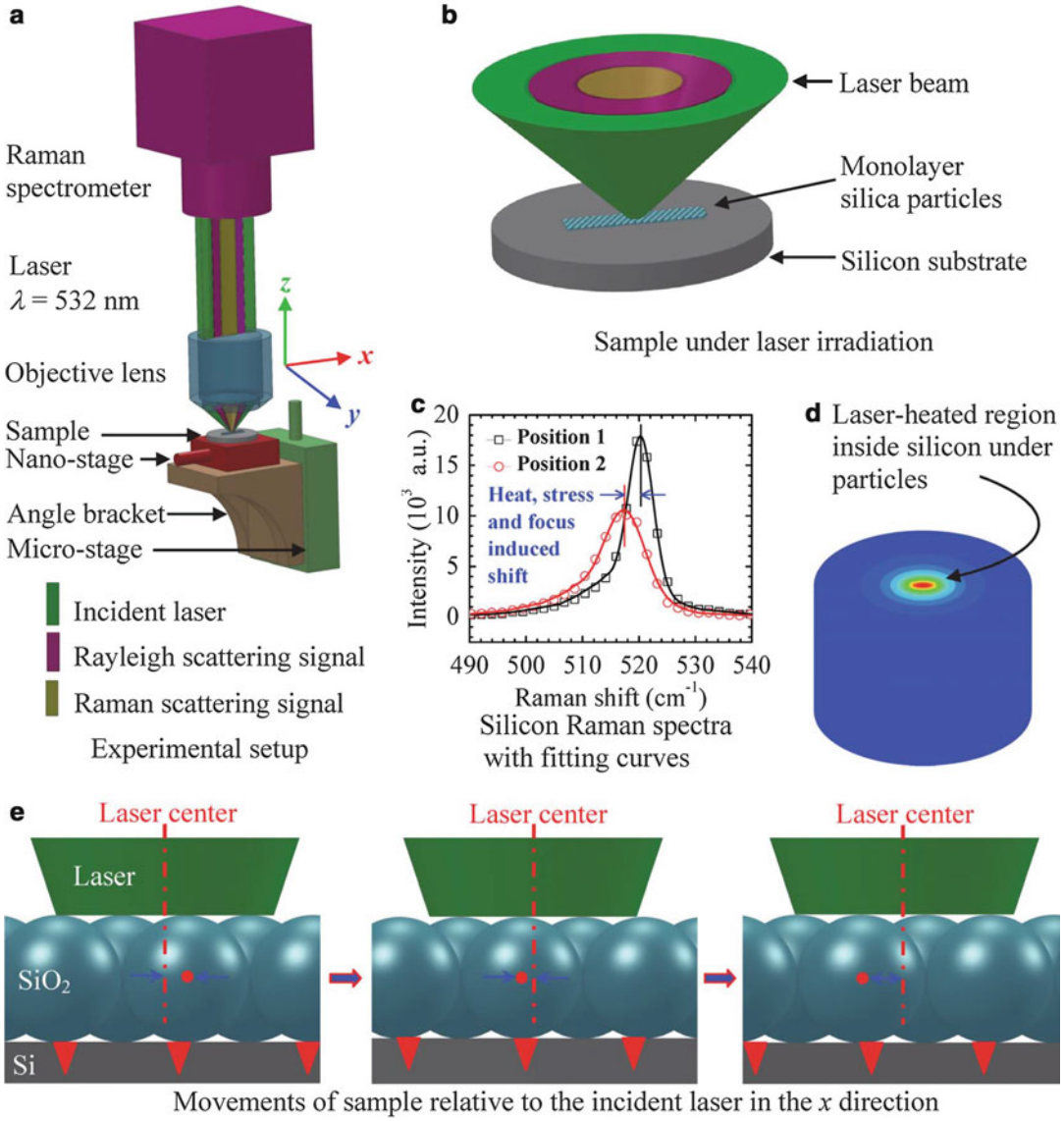

Fig. 5 Schematic of experimental setup for far-field nanoscale imaging (not to scale). (**a**) A sample is located under an objective-focused laser beam from a Raman spectrometer. The movement of sample in the *x* direction is controlled by a piezo-actuated nanostage. The focal level of the laser on the sample in the *z* direction is controlled by a motorized microstage. (**b**) The sample consists of a silicon substrate and a monolayer of silica particles. The spot size of the incident laser is about 0.5 μm in the *x*–*y* plane on a silicon substrate. (**c**) The Raman spectrum shifts to left due to the near-field laser heating, the stress, and the out-of-focus effect. (**d**) The silicon substrate is heated in a sub-wavelength region ($r \sim 200$ nm) right beneath the particles. (**e**) During the experiment, the position of the laser beam is fixed, and the sample moves along the *x* direction controlled by the nanostage electrically without any touch of the sample and other equipment. The step of movement is 27 nm in a range of about 4 μm (Reprinted with permission from reference [8])

Details can be found in reference [8]. The experimental setup for temperature, stress, and optical field mapping is shown in Fig. 5. The sample is mounted on a combined stage under the confocal Raman system (VoyageTM, B&W Tek, and Olympus BX51): a piezo-actuated nanostage with a resolution of 20 nm (ThorLabs NFL5DP20) in the *x* direction (imaging direction) and a motorized translation stage (ThorLabs MT1-Z8) in the *z* direction. The mapping process is conducted along the *x* direction. The motorized stage is fixed tightly to exclude the movement in the *z* direction. The Raman laser is the only laser source used for both near-field excitation and probing, which is focused on the top of glass

DOI 10.1007/978-94-007-6178-0_100915-1

nanoparticles by a 100× objective lens (NA = 0.8). When passing through the SiO_2 particle, the laser is further focused to an even smaller spot size. Temperature and stress mapping are carried out by measuring Raman spectra along the *x* direction. Four energy levels of incident laser are applied in the experiment.

De-conjugation of Thermal, Stress, and Optical Effects

The obtained Raman spectra are first fitted using the Gaussian function to get the precise Raman intensity, Raman shift, and linewidth. Raman intensity, Raman shift, and linewidth of the Si peak will vary against temperature. The Raman intensity and shift decrease, while the linewidth broadens as the temperature rises. Among these three parameters of the Raman peak, the linewidth is closely relevant to the phonon lifetime. It is strongly affected by the temperature in collection area, but the stress has little effect on it. Therefore, the linewidth method is available for direct temperature analysis. Raman shift depends on both the local stress and temperature, and Raman intensity is mainly affected by the intensity of the incident laser and the temperature of the silicon substrate. The optical field intensity variation and the stress distribution can be obtained through analyzing Raman intensity and shift, respectively. Therefore, the periodic variation of the combined effect of the near-field optical heating, local stress, and the optical field in space can be separately detected by analyzing the variation of the Raman intensity, Raman shift, and linewidth along the mapping path.

The optical alignment in the system and laser energy will affect the Raman intensity, but they are independent of the sample. To quantitatively obtain the nanoscale local stress and temperature in the silicon substrate based on the intensity in this particle–substrate model, the Raman spectrum for bare silicon is referred at the same measurement condition. The effect induced by the incident laser can be eliminated when the Raman intensity ratio from silicon under particles to that from bare silicon, I_{SiO2}/I_{Si}, is applied. The difference between I_{SiO2} and I_{Si} is caused by the temperature rise under the irradiation. The silica particle-induced near-field focusing effect largely raises the temperature of the silicon substrate in the probed area. The intensity ratio I_{SiO2}/I_{Si} is then normalized by dividing the extrapolation value at 0 laser energy $[I_{SiO2}/I_{Si}]_{E=0}$. The normalized intensity ratio $[I_{SiO2}/I_{Si}]/[I_{SiO2}/I_{Si}]_{E=0}$ reduces when energy flux increases. With the calibration of I_{Si} against temperature, the temperature rise ΔT induced by 1,210 nm particles are obtained from 10.0 to 56.1 K with an uncertainty of ±7.0 K, when the laser energy percentage goes from 25 % to 100 %.

The thermal stress σ inside the silicon under particles is then determined by using both Raman shift ω and linewidth Γ. Due to the fact that Γ is less sensitive to stress than ω, the experimental linewidth and Raman shift can be expressed as $\Delta\Gamma_{exp} = \Delta\Gamma_{\Delta T} + \Delta\Gamma_{focus}$ and $\Delta\omega_{exp} = \Delta\omega_{\Delta T} + \Delta\omega_{focus} + \Delta\omega_{\sigma}$, respectively, when the temperature rise and out-of-focus effect induced by the particles are considered. With the slopes for linewidth and Raman shift against temperature increase in the calibration and the calculated ΔT from intensity, $\Delta\Gamma_{focus}$ can be easily obtained. Another calibration is conducted to obtain the relationship between $\Delta\Gamma_{focus}$ and $\Delta\omega_{focus}$ induced by the out-of-focus effect: $\Delta\omega_{focus} = -0.21–0.77\Delta\Gamma_{focus}$. Thus, $\Delta\omega_{\sigma}$ and even σ can be both obtained easily. A proportionality constant of $-3.6\ cm^{-1}$/GPa [11] is adopted for calculating the stress σ inside silicon based on the variation of Raman shift $\Delta\omega_{\sigma}$. According to the calculation, σ increases from 140 to 370 MPa with an uncertainty of 640 MPa as the energy percentage of laser goes up from 25 % to 100 %.

The cases of silicon under particles of smaller sizes, 800, 400, and 200 nm, are also studied. It is found that the maximum Raman intensity ratio (I_{max}/I_{min}) decreases as the particles decreases from 1,210 to 160 nm. 140 nm diameter particles would be the minimum size which can be detected by using this confocal Raman system. The lateral resolution improves with the increase of the particle size. The best resolution of about 20 nm is achieved when the particle diameter is 1,210 nm.

DOI 10.1007/978-94-007-6178-0_100915-1

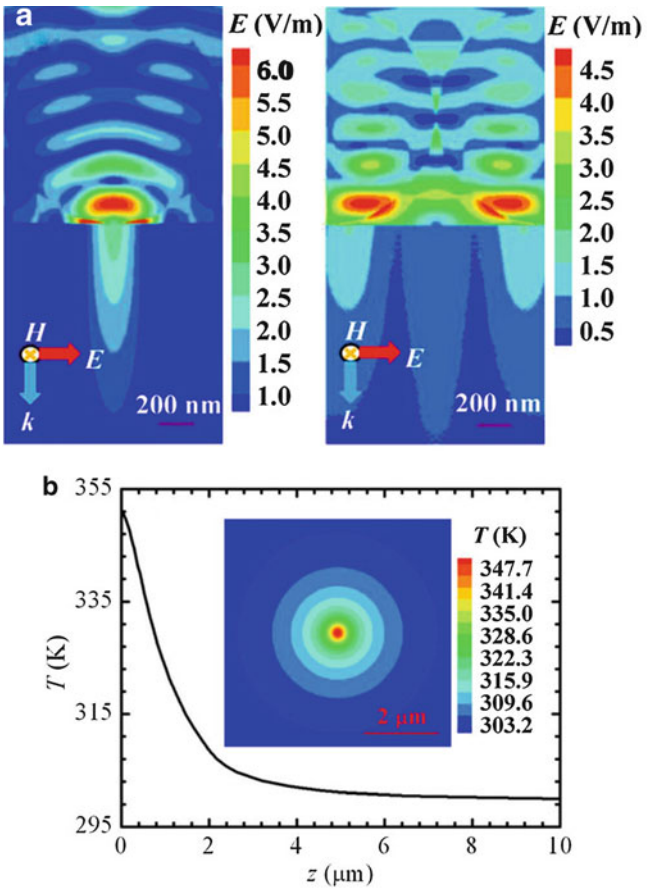

Fig. 6 (**a**) HFSS modeling of a plane wave passing through a 1.21 μm silica sphere (e = 2.13 + 0i) in air above a silicon substrate (e = 17.22 + 0.428i). The amplitude of electric field is equal to the enhancement factor. In the left figure, the particle center is under the laser spot center. In the right figure, the particle center is at the fringe of the laser spot area. (**b**) Temperature profile inside a silicon substrate beneath a 1210 nm silica particle under laser irradiation. The *inset* shows the temperature distribution on the top of the substrate (Reprinted with permission from ref. [8])

Near-Field Thermal, Optical, and Mechanical Phenomena: Modeling

The 1,210 nm particle–substrate case is also studied with the finite element method by using HFSS (V14 ANSYS, Inc) [8–10]. A quarter of the silica particle and the substrate are used due to the consideration of the amount of mesh density and calculation in HFSS. A plane wave (λ = 532 nm) irradiates normally from the top of the particle. In the experiment, the laser spot size is smaller than the diameter of the 1,210 nm particle. To meet the experimental condition, only the parts of particles inside the laser spot area remain in the model. The rest parts are cut off to avoid receiving the plane wave. Perfect H and Perfect E symmetry boundaries are applied for symmetrical planes. Absorbing (radiation) boundaries are applied for other boundary planes in the domain. Two typical cases regarding different laser-particle positions in an imaging period are simulated, and the resulting electric field distribution is shown in Fig. 6a.

The temperature distribution inside the silicon substrate is calculated by using FLUENT (V12.0. 1 ANSYS, Inc) based on the electric field distribution. Because of the symmetry of the temperature distribution inside the silicon, a quarter cylinder computational domain with a radius of 5 mm and a height of 10 mm is adopted in the simulation. Both vertical cross sections use symmetrical boundary conditions and the top surface is set as adiabatic. The temperature of peripheral and bottom surfaces of the domain

DOI 10.1007/978-94-007-6178-0_100915-1

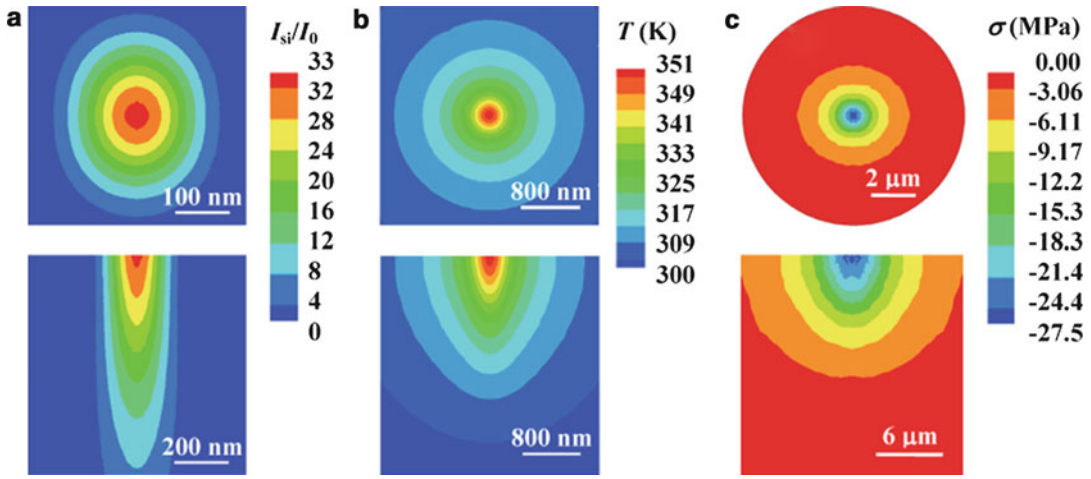

Fig. 7 (**a**) Optical intensity distribution inside the silicon substrate. The amplitude indicates the optical intensity enhancement relative to the incident wave. (**b**) Temperature distribution inside the silicon substrate. The initial temperature in silicon is 300 K. (**c**) The thermal stress distribution induced by temperature rise inside the silicon substrate. The upper figures show the top of the substrate, and the lower figures show the vertical planes (side view) in silicon under the particle center (Reprinted with permission from ref. [9])

and the initial temperature of the substrate are set at 300 K. The calculated temperature profile in the silicon substrate beneath the silica particle is shown in Fig. 6b.

The stress distribution in the silicon substrate beneath a single silica particle is also studied [9]. The thermal stress distribution inside the silicon substrate (Fig. 7) is simulated with ANSYS V14. The model as well as the temperature distribution is imported from the FLUENT calculation. The peripheral and foot end surfaces of the model are fixed. The top boundary is not constrained. Both vertical cross sections are symmetrical. The calculated maximum thermal stress in the single particle case is around 30 MPa, which is much lower than the experimental value (160 Mpa) determined from Raman shift and linewidth. The difference between the experiment and the simulation is mainly induced by the setting of the incident laser and the out-of-focus effect in experiment.

Material Structure Evolution Under Near-Field Laser Heating

In laser-assisted STM nanostructuring, as a direct consequence of nanoscale heating, the nanodomain of a sample just below the STM tip experiences intense heating, phase change, phase explosion, stress development and propagation, and rapid structural evolution. The enhanced optical field, light confinement, and only the thermal evolution of the sample surface under the STM tip without phase change have been widely studied. Furthermore, in surface nanostructuring, the final surface nanostructure is strongly affected by solidification of the molten material. The solidification process is driven by the heat conduction in the material and is much slower than the heating and melting processes that are largely driven by the laser energy input. Previous works mainly focused on the simulation in a small scale and short time duration. In this section, studies for a longtime behavior of a large system consisting of more than one hundred million atoms are introduced for the material structure evolution: heating, melting, phase change, solidification, and defect formation in the laser-assisted STM nanostructuring. The model used in the simulation is designed with true dimensions though the simulated result is based on several artificial assumptions.

DOI 10.1007/978-94-007-6178-0_100915-1

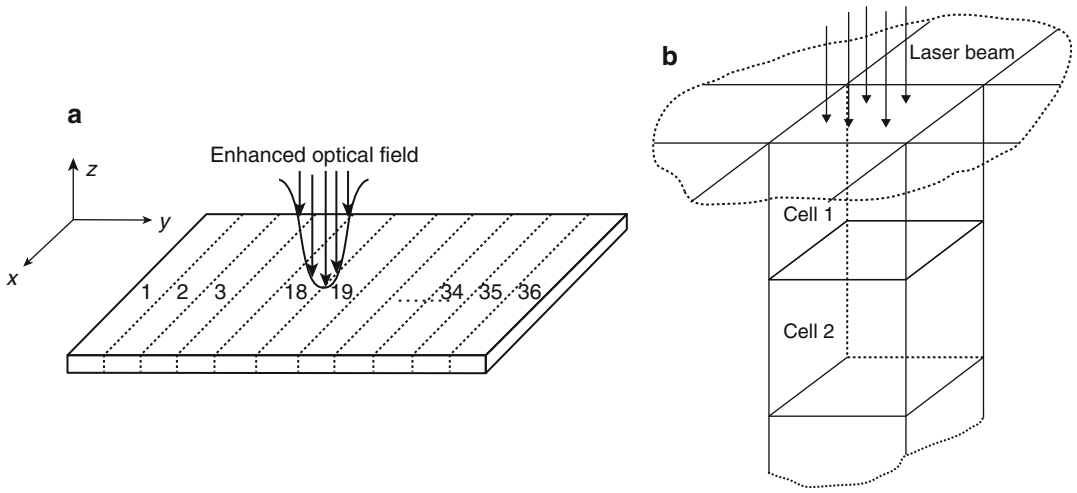

Fig. 8 (**a**) Schematic of the MD configuration. (**b**) Schematic of the laser beam absorption in the material (Reprinted from ref. [14], © IOP Publishing. Reproduced by permission of IOP Publishing. All rights reserved)

Methodologies of Large-Scale Parallel Molecular-Dynamics (MD) Simulation

At nanoscale, the thermal movements of molecules/atoms show strong statistical variations in space since thermal equilibrium cannot be well established. MD simulation, which directly tracks the movement of molecules/atoms, is capable of exploring the physical phenomena down to molecular/atomic levels. A designed thin freestanding argon film at 50 K is irradiated with a near-field focused laser beam. The distribution of the optical field in space and time for this laser beam is constructed as

$$I = I_0 \exp\left(\frac{-\left(\vec{r} - \vec{r}_0\right)^2}{r_g^2}\right) exp\left(\frac{-(r - r_0)^2}{r_g^2}\right), \tag{1}$$

where I_0 is a laser beam intensity constant, r is the location of the laser beam, r_0 is the center of the sample surface, r_g is a length constant determining the size of the laser beam, t is the time, t_0 is a time constant determining the peak location of the laser intensity in the time domain, and t_g is a time constant determining the pulse width of the laser beam.

To simulate the laser–argon film interaction, the movement of atoms is governed by the Newtonian equation,

$$m_i \frac{d^2 r_i}{dt^2} = \sum_{j \neq i} F_{ij}, \tag{2}$$

where m_i and r_i are the mass and position of atom i, respectively. F_{ij} is the interaction force between atoms i and j and is computed from the Lennard-Jones (LJ) potential as $F_{ij} = -\partial\phi_{ij}/\partial r_{ij}$. The Lennard-Jones potential ϕ_{ij} follows the form

$$\phi_{ij} = 4\varepsilon\left[\left(\frac{\sigma_e}{r_{ij}}\right)^{12} - \left(\frac{\sigma_e}{r_{ij}}\right)^{6}\right], \tag{3}$$

DOI 10.1007/978-94-007-6178-0_100915-1

The half-step leapfrog scheme is used in the simulation. For argon, the cutoff distance r_c adopts the widely accepted value $2.5\sigma_e$. Computation of the force between an atom and its neighbors is arranged by the cell structure and the linked-list method.

When studying the longtime behavior of a large system, the physical domain is divided into N subdomains of the same size as shown in Fig. 8a, and these subdomains are distributed over a parallel computer consisting of N computing nodes. Each node is responsible for the MD simulation of one subdomain. The parallel program is developed using MPICH. Periodical boundary conditions are applied to the boundaries in the x and y directions and free boundary conditions to the boundaries in the z direction. Details of the parallel treatment are discussed in reference [12]. Nowadays, various MD simulation packages are available for parallel computation. Still this subdomain scheme saves significant time for data exchange among computing nodes.

The numerical treatment of the laser absorption in the sample is shown in Fig. 8b. The MD domain is divided into cubic cells with a little larger size than cutoff distance. Take cells 1 and 2 as examples; cell 1 is the first cell to absorb the laser energy when the laser propagates from one layer to another along the z direction. The laser energy absorbed by cell 1 within each time step is

$$\delta E_1 = E_1\left(1 - exp\left(\frac{-\delta z}{\tau_1}\right)\right), \tag{4}$$

where E_1 is the laser energy reaching cell 1 within one time step $\delta t, E_1 = \int_A I\delta t \cdot dA$. δz is the z dimension of cell 1. τ_1 is the modified artificial absorption depth due to heating, explosion, and other physical processes. The artificial absorption depth is designed to reflect the volumetric absorption of the laser beam in the sample rather than to represent the practical experimental condition. When laser arrives at cell 2, the energy is $E_2 = E_1 - \delta E_1$. The laser energy absorbed by cell 2 can be calculated with eqn. 4. The laser keeps propagating and the energy absorption process is continued in the following cells until the energy is totally absorbed. The kinetic energy of atoms in the material is excited by the energy transferred from the laser beam, while the momentum of atoms is conserved during laser energy absorption.

The Material Structure Evolution: Heating, Melting, Phase Change, Solidification, and Defect Formation

The solidification and crystallization of an argon film of 100,776,960 atoms is simulated over 2 ns [13] after the irradiation of a near-field enhanced pulse laser. The film is comprised of 648 fcc unit cells (350.83 nm) in the x and y directions and 60 fcc unit cells (32.48 nm) in the z direction. The length of the film is much larger than the beam spot of 25 nm, and the thickness is much thicker than the optical absorption depth 10 nm. The pulse energy is taken as 8×10^{-15} J, which corresponds to an energy density level of 50 MW/cm^2. Before applying laser heating, the simulation is run for 100 ps, during which the velocity of atoms is scaled to make the sample to reach 50 K gradually. After this velocity scaling, the sample is simulated for another 100 ps to eliminate the disturbance introduced by the velocity scaling. Free spaces are added below and above the sample to capture the movement of atoms escaping from the sample. The entire computational domain measures 350.83 nm in the x and y directions and 759.10 nm in the z direction with the back side of the sample located at 213.71 nm.

Epitaxial regrowth process is observed in this longtime simulation. The atomic dislocation is induced by thermal strain in the epitaxial regrowth. The normal compressive stress and negligible shear stress decline when the melting occurs. The distance between atoms is studied to reflect the crystallinity and distinguish solid and liquid. The solid–liquid interface moves at an average speed of 3–5 m/s which increases with time, and the spatial distribution of the moving speed at the solid–liquid interface in

DOI 10.1007/978-94-007-6178-0_100915-1

nonuniform. Two edges of the liquid region in the nanohole solidify first, and their solidification speed is faster than that at the bottom because the heat conduction area at the two edges is much stronger, which leads to the appearance of nonuniform epitaxial regrowth.

Irregular perturbations at the edge of the nanohole are observed in simulating the surface nanostructuring with a pulse-laser-assisted STM [14]. To explore the thermal and mechanical mechanisms, another system consisting of more than 200 million atoms is modeled by employing large-scale parallel MD simulations. The sample is designed as 648 fcc unit cells (350.83 nm) in the x and y directions and 60 fcc unit cells (32.48 nm) in the z direction. The pulse energy is taken as 1.6×10^{-14} J, which corresponds to an energy density level of 100 MW/cm^2. Strong compressive stress develops beneath the sample surface due to the absorption of the strong laser power. These compressive stresses then drive atoms' movement to induce phase explosion. In addition, the anisotropic propagation of the stress occurs in the material because of the direction-dependent stress wave speeds in the crystal. Visible subsurface structural damages are observed in the direction of 45° with respect to the z axis. The strong tensile stress resulting from the reflection of the compressive stress at the bottom plays the most significant role in inducing the structural damage.

The solidification process of the nanohole after laser heating is also studied by varying the power of the pulse laser [15]. The MD simulation is performed on a very small surface area (tens of nanometers in diameter) in argon crystals, with eight different levels of laser beam energy input: 0.05, 0.1, 0.2, 0.35, 0.5, 0.75, 1, and 1.1 fJ. The corresponding maximal energy density levels are about 12, 24, 48, 84, 120, 180, 240, and 260 MW/cm^2, respectively. The detailed sizes of simulated domains are listed in Table 1. The effect of stress reflection from the bottom of the sample on the final nanostructure is reduced by using suitable large domain size. The diameter, depth, and edge protrusion of the nanohole increase when the laser fluence slows down. The largest melting thickness is reached after the laser heating stops because the melting procedure still continues due to the fact that heat conduction is continuing and its rate is much lower than the heating speed.

Shock Wave

During the process of laser-assisted SPM nanostructuring, intense laser heating will make the solid-state material transfer directly into gas phase to result in phase explosion. The ejected atoms have high kinetic energy and movement speed. When an ambient gas is present, this high-speed movement could compress ambient gas atoms in a very short time, leading to a strong shock wave. It is a very important phenomenon though it is little useful in nanomanufacturing. The first atomistic modeling work on shock wave was done by Zhang et al. [16] in picosecond laser–material interaction. The formation of the shock wave in the nanoscale domain could significantly affect the laser–material interacting zone and the nanostructuring process.

In the shock wave phenomena, the kinetic and physical properties of the disturbed gas compression are explored in a nanodomain in near-field laser–material interaction [17]. The gas compression is driven by the high-speed movement of the molten particulates ejected from the solid target in a nanodomain. The quick interaction between solid and gas atoms compresses the gas and forms a steep shock wave front, which moves at a supersonic speed. The fast compression of gas also induces a steep interface of density, temperature, and pressure distribution, which are viewed as typical characteristics of nanoscale shock waves. Evolutions of shock wave front position, velocity, and Mach number are shown in Fig. 9, illustrating quick decay during wave propagation. Because of energy dissipation, the temperature, pressure, and speed of the shock wave experience a fast decay, but the Mach number always remained higher than 1, meaning the shock wave always persisted in the simulation.

A one-dimensional model is established to simply describe the shock wave front in nanosecond laser–material interaction. The longtime phase change, including solid–liquid interface speed,

Table 1 Detailed information about the three domains studied

	Sample 1	Sample 2	Sample 3
FCC cubes in the domain ($x \times y \times z$)	$5 \times 324 \times 60$	$5 \times 648 \times 60$	$5 \times 324 \times 120$
Domain size (nm^3)	$2.707 \times 175.4 \times 32.48$	$2.707 \times 350.8 \times 32.48$	$2.707 \times 175.4 \times 64.97$
Atom number	388,800	777,600	777,600

Reprinted from reference [15], Copyright (2008), with permission from Elsevier

DOI 10.1007/978-94-007-6178-0_100915-1

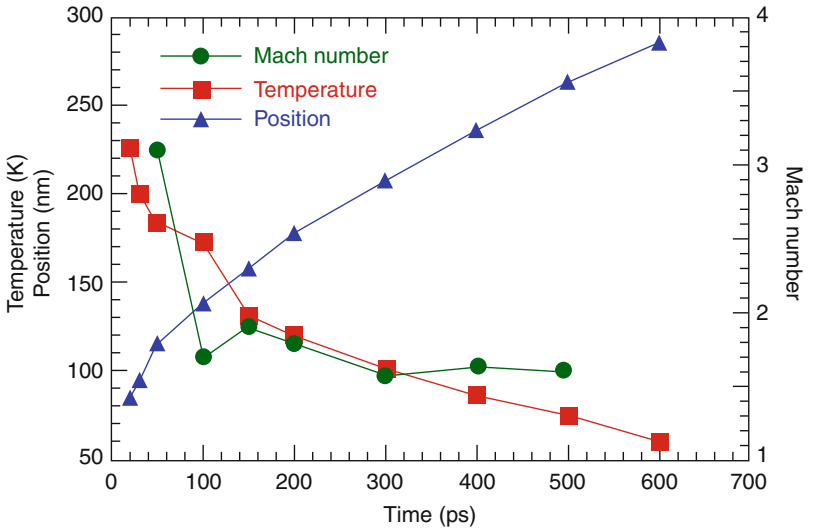

Fig. 9 Evolution of the shock wave front temperature, position, and Mach number against time (Reprinted from ref. [17], Copyright (2007), with permission from Elsevier)

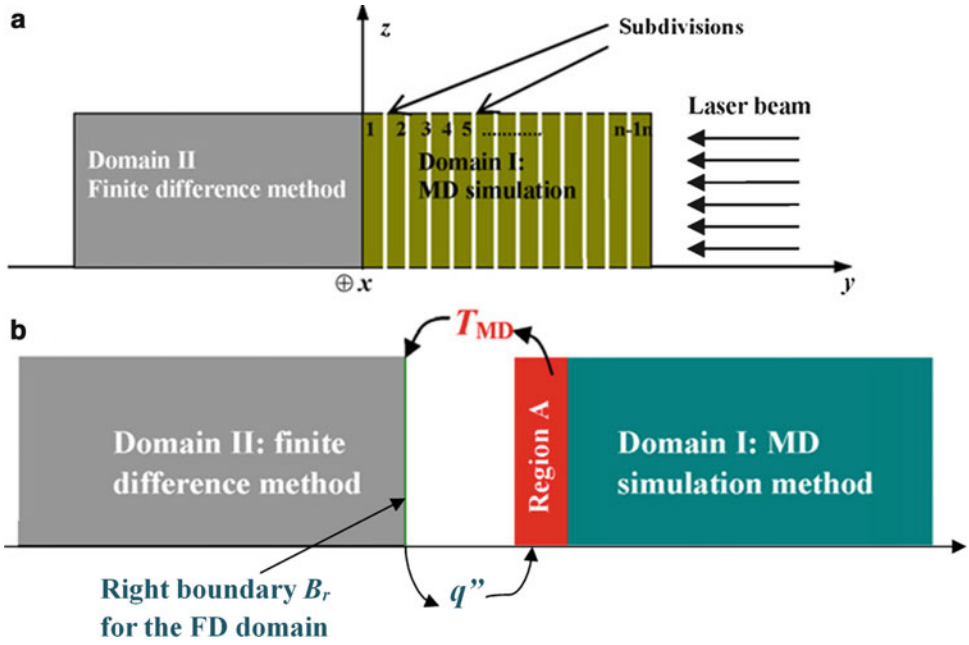

Fig. 10 (**a**) Schematic of the computational domain; (**b**) schematic for treatment of the interface between the MD and FD domains (Reprinted from ref. [18], Copyright (2008), with permission from Elsevier)

temperature, maximum melting depth, and ablation rate, is systematically studied [18]. The whole modeled domain is divided into two subdomains as shown in Fig. 10. Subdomain I is directly subjected to the nanosecond laser irradiation, and its length along the *y* direction is much longer than the laser melting depth. Subdomain II only experiences heat conduction, and its length is longer than the thermal diffusion length in the material. Subdomain I and II are simulated with finite difference method and MD method, respectively. The temperature and heat flux are continuous at the interface. Periodical boundary conditions are used along the *x* and *z* directions as shown in Fig. 10. Strong fluctuation is observed at the

DOI 10.1007/978-94-007-6178-0_100915-1

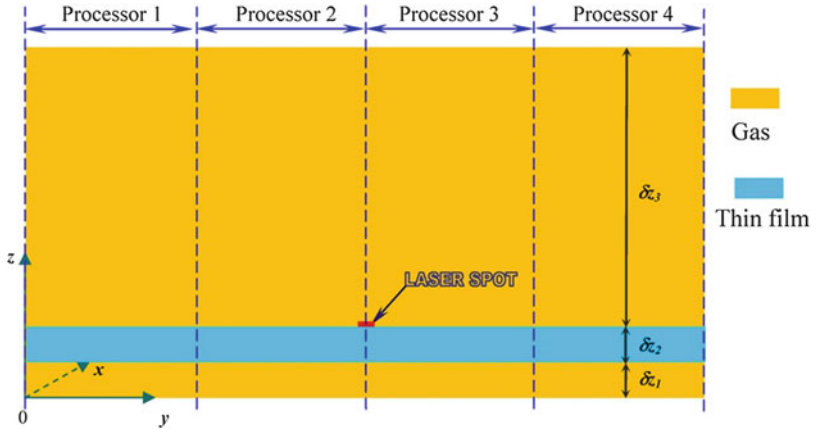

Fig. 11 Schematic of the MD configuration for shock wave study and parallel computation (Reprinted from ref. [19], © IOP Publishing. Reproduced by permission of IOP Publishing. All rights reserved)

Table 2 Conditions, domain sizes, and total number of atoms for different cases

Group	Conditions	δz_1 (nm)	δz_1 (nm)	δz_1 (nm)	l_x (nm)	l_y (nm)	N
1	$\beta = 2, \gamma = 1$	21.656	32.484	541.4	2.707	920.38	2480960
	$\beta = 1, \gamma = 1$	21.656	32.484	541.4	2.707	920.38	2480960
	$\beta = 0.5, \gamma = 1$	21.656	32.484	541.4	2.707	920.38	2480960
	$\beta = 0.25, \gamma = 1$	21.656	32.484	541.4	2.707	920.38	2480960
	$\beta = 0.125, \gamma = 1$	21.656	32.484	541.4	2.707	900.89	2429440
2	$\beta = 1, \gamma = 0.25$	34.650	34.650	1732.479	2.707	900.89	2469376
	$\beta = 1, \gamma = 0.0626$	34.650	34.650	1732.479	2.707	900.89	2214784
	$\beta = 1, \gamma = 0.0157$	34.650	34.650	1732.479	2.707	900.89	2151136

Reprinted from reference [19], © IOP Publishing. Reproduced by permission of IOP Publishing. All rights reserved

solid–liquid interface and surface of the molten pool. No visible superheating is observed at the solid–liquid interface. The melting stops later. A higher peak melting speed appears with higher laser fluence. An almost linear relationship is observed between the ablation yield and the laser fluence, indicating weak phase explosion.

The properties of background gas also have effects on the shock wave [19, 20]. The molecular weight and density of background gas are considered on the laser-induced shock wave. A quasi-three-dimensional model (Fig. 11) is constructed to study a free argon thin film in a gas environment. This simulated system consists of over 2 million atoms so the parallel computation is employed. Eight cases of different background gases are studied in two groups. Details are listed in Table 2. The lower ambient pressure or lighter background gas causes the larger area being affected and a weaker shock wave front. The molecular weight of background gas has little effect on the final kinetic energy of the ablated material and the energy of the background gas regardless of the ambient pressure and laser fluence. When the ambient pressure is reduced, more kinetic energy is carried out by the ablated material, while less energy is transferred to the ambient gas. By studying the ablation in the temporal domain, a heavier ambient gas is observed to bounce back the ablated material.

DOI 10.1007/978-94-007-6178-0_100915-1

Concluding Remarks

The experimental and computational works mainly focus on the laser-assisted tip–substrate interaction. The near-field focus effect largely enhances the optical field in the substrate under the tip other than inside the tip. The large parallel MD simulations are carried out to study longtime surface evolution after an intensive pulse applied on it including material structure evolution: heating, melting, phase change, solidification, and defect formation. A shock wave is observed and systematically studied. The effect of gas background is also considered.

There are some problems still faced in nanomanufacturing. The nanostructuring is a dynamic process, and the processing area is very small (low to the nanoscale). The phenomena occurring in this area are difficult to observe and measure. In the SPM tip-assisted nanomanufacturing, the near-field effect will be easily changed due to vulnerable tip. Either the bump damage or the contamination of the apex of the tip will broaden the tip and finally changes the near-field optical field distribution in and around the tip. Furthermore, in this tip–substrate system, the tip and the substrate are so close to be considered in contact with each other. Therefore, any thermal expansion from the tip and the substrate induced by the local laser heating will result in measurement instability. Right now the measurement for laser-assisted tip-based nanomanufacturing takes a longer time compared to the time of the dynamic process in the manufacturing. The manufacturing is confined in the nanoscale as well. Future improvement of this technique is required to develop the quick response of the measurement and scale up the manufacturing and improve the scalability in industries.

Cross-References

- ▶ Heat
- ▶ Heat Capacity
- ▶ Heat Conduction
- ▶ Heat Conductivity
- ▶ Molecular Dynamics Method
- ▶ Nanofabrication
- ▶ Nanoscale Heat Transport
- ▶ Nano-Scale Structuring
- ▶ Nanoscale Thermal Analysis
- ▶ Nanotechnology
- ▶ Near-Field Optics
- ▶ Near-Field Scanning Optical Microscopy (NSOM)
- ▶ Thermal Conductance
- ▶ Thermal Resistance
- ▶ Thermal Transport
- ▶ Thermometry

References

1. Lu, Y.F., Hu, B., Mai, Z.H., Wang, W.J., Chim, W.K., Chong, T.C.: Laser-scanning probe microscope based nanoprocessing of electronics materials. Jpn. J. Appl. Phys. **1**(40), 4395–4398 (2001)

2. Chen, X.W., Wang, X.W.: Near-field thermal transport in a nanotip under laser irradiation. Nanotechnology **22**, 075204 (2011)
3. Chen, X.W., Wang, X.W.: Microscale spatially resolved thermal response of Si nanotip to laser irradiation. J. Phys. Chem. C **115**, 22207–22216 (2011)
4. McCarthy, B., Zhao, Y.M., Grover, R., Sarid, D.: Enhanced Raman scattering for temperature measurement of a laser-heated atomic force microscope tip. Appl. Phys. Lett. **86**, 111914 (2005)
5. Yue, Y.A., Chen, X.W., Wang, X.W.: Noncontact Sub-10 nm temperature measurement in near-field laser heating. ACS Nano **5**, 4466–4475 (2011)
6. Downes, A., Salter, D., Elfick, A.: Finite element simulations of tip-enhanced Raman and fluorescence spectroscopy. J. Phys. Chem. B **110**, 6692–6698 (2006)
7. Chen, G.: Nonlocal and nonequilibrium heat conduction in the vicinity of nanoparticles. J. Heat Trans-T. ASME **118**, 539–545 (1996)
8. Tang, X.D., Xu, S., Wang, X.W.: Nanoscale probing of thermal, stress, and optical fields under near-field laser heating. Plos One **8**, e58030 (2013)
9. Tang, X.D., Xu, S., Wang, X.W.: Thermal probing in single microparticle and microfiber induced near-field laser focusing. Opt. Express **21**, 14303–14315 (2013)
10. Tang, X.D., Yue, Y.N., Chen, X.W., Wang, X.W.: Sub-wavelength temperature probing in near-field laser heating by particles. Opt. Express **20**, 14152–14167 (2012)
11. Beechem, T., Graham, S., Kearney, S.P., Phinney, L.M., Serrano, J.R.: Invited article: simultaneous mapping of temperature and stress in microdevices using micro-Raman spectroscopy. Rev. Sci. Instrum. **78**, 061301–9 (2007)
12. Wang, X., Lawrence, C.: In: Proceedings of the ASME heat transfer/fluids engineering summer conference 2004. Charlotte, NC. American Society of Mechanical Engineers, New York, 2004
13. Wang, X.W., Lu, Y.F.: Solidification and epitaxial regrowth in surface nanostructuring with laser-assisted scanning tunneling microscope. J. Appl. Phys. **98**, 114304 (2005)
14. Wang, X.W.: Large-scale molecular dynamics simulation of surface nanostructuring with a laser-assisted scanning tunnelling microscope. J. Phys. D Appl. Phys. **38**, 1805–1823 (2005)
15. Feng, X.H., Wang, X.W.: Effects of laser fluence on near-field surface nanostructuring. Appl. Surf. Sci. **254**, 4201–4210 (2008)
16. Zhang, L.J., Wang, X.W.: Dynamic structure and mass penetration of shock wave in picosecond laser-material interaction. Jpn. J. Appl. Phys. **47**, 964–968 (2008)
17. Feng, X.H., Wang, X.W.: Nanodomain shock wave in near-field laser-material interaction. Phys. Lett. A **369**, 323–327 (2007)
18. Zhang, L.J., Wang, X.W.: Hybrid atomistic-macroscale modeling of long-time phase change in nanosecond laser-material interaction. Appl. Surf. Sci. **255**, 3097–3103 (2008)
19. Guo, L.Y., Wang, X.W.: Effect of molecular weight and density of ambient gas on shock wave in laser-induced surface nanostructuring. J. Phys. D Appl. Phys. **42**, 015307 (2009)
20. Li, C., Zhang, J.C., Wang, X.W.: Phase change and stress wave in picosecond laser-material interaction with shock wave formation. Appl. Phys. A-Mater. **112**, 677–687 (2013)